Enhanced activity and durability of FeCoCrMoCBY nanoglass in acidic hydrogen evolution reaction

Mengyang Yan [a], Shuangqin Chen [a, *], Shangshu Wu [a], Xuechun Zhou [a], Shu Fu [a], Di Wang [b], Christian Kübel [b], Horst Hahn [a, b], Si Lan [a, *], Tao Feng [a, *]

[a] Herbert Gleiter Institute of Nanoscience, School of Material Science and Engineering, Nanjing University of Science and Technology, Nanjing 210094, China
[b] Institute of Nanotechnology, Karlsruhe Institute of Technology, Karlsruhe 76021, Germany

Keywords:
Nanoglass
Inert gas condensations
High energy states
Hydrogen evolution reactions

A B S T R A C T

In the present work, a multi-element nanoglass (m-NG) of FeCoCrMoCBY is obtained first time by the laser ablation combined with inert gas condensation (laser-IGC) technique. Compared with the conventional rapid-quenched metallic glass (MG) with identical composition, the Fe-based m-NG demonstrates a superior performance as a self-supported electrocatalyst for hydrogen evolution reaction (HER) in acidic solution. The enhanced HER activity of m-NG is proposed to be closely related to its high energy states, which is originated from the unique inhomogeneous nanostructures with a high density of low-coordinated atoms. Additionally, the Fe-based m-NG exhibits an outstanding comprehensive catalytic performance even beyond the commercial Pt/C catalyst in long-term test due to its self-optimization ability. This work not only opens the way to the preparation of m-NGs by the novel laser-IGC technique, but also makes a great contribution to developing low-cost, high-efficient, and super-durable HER electrocatalysts in acidic environment.

1. Introduction

Acidic water electrolysis is a well-matured technique for hydrogen production due to the high current densities, high voltage efficiency, and rapid responses compared with the alkaline methods [1–3]. However, the harsh corrosive environment requires efficient catalysts with the capabilities to resist acidic corrosion and sustain large current densities. Only some noble metals such as Pt, Ir, and Ru, have been successfully applied in industrial production. As the scarcest elements in the world, the high price and large consumption of noble catalysts restrict the widespread utilization of this technology, leading to a critical demand for acidic electrocatalysts consisting of earth-abundant elements [4,5].

Metallic glasses (MGs), as a category of metastable materials with amorphous structures, possess superior properties to the crystalline counterparts, especially for electrochemical catalysis. The high energy states [6–8] and chemically isotropic microstructures [9,10] strengthen the catalytic capability and corrosion resistance of MG compared with the corresponding crystalline alloys. Consequently, the MGs have been suggested as high-performance catalysts and attracted considerable attention recently. For example, MGs with the composition of $Ni_{40}Fe_{40}P_{20}$ [7], $Fe_{40}Co_{40}P_{13}C_7$ [11], and $Pd_{40}Ni_{10}Cu_{30}P_{20}$ [12] exhibited outstanding performances in hydrogen evolution reaction (HER) and oxygen evolution reaction (OER). Fe-based MGs like $Fe_{78}Si_9B_{13}$ [13] were proven to have excellent catalytic properties in wastewater remediation involving oxidative degradation of organic pollutants. The Pt- and Pd-based MGs with outstanding corrosion resistance and high conductivity presented superior catalytic performances in methanol and ethanol oxidation reactions [14–16].

Although MGs exhibit great potential for electrochemical catalysis, it remains a big challenge to furtherly enhance the activity and durability of MG electrocatalysts for practical applications. It is well known that inhomogeneous defects such as steps, kinks, and edges are significant for crystalline catalysts [17]. Tailoring the defects through defect engineering methods, such as etching, doping, dealloying, and ion intercalation, has been recognized as a universal strategy to optimize the performance of crystalline electrocatalysts. For example, vapor phase and electrochemical dealloying methods have been widely utilized in fabricating high-performance porous electrocatalysts for water splitting [18,19]. However, owing to the long-range homogeneous amorphous structures, it is difficult to introduce “defects”, like grain boundary in crystals, into the amorphous matrix using post-treatment processes. Numerous

* Corresponding authors.
E-mail addresses: chensq-hgi@njust.edu.cn (S. Chen), lansi@njust.edu.cn (S. Lan), tao.feng@njust.edu.cn (T. Feng).

strategies, such as severe plastic deformation [20, 21], ion irradiation [22], and cryogenic thermal cycling [23], have been thoroughly studied to overcome this barrier in recent years. For example, high-pressure torsion has been applied on MG ribbons with compositions of $Pd_{40}Ni_{10}Cu_{30}P_{20}$ [24] and $Fe_{78}Si_9B_{13}$ [25, 26] to introduce internally defective structures, leading to the enhancement of HER and OER activity, respectively. However, these methods still face many problems such as small sample size, high energy consumption, and possible crystallization, limiting the widespread fabrication and utilization.

In order to resolve this challenge, a novel bottom-up method has been developed to synthesize MG with endogenously inhomogeneous nanostructures, which is named as nanoglass (NG). NGs consist of amorphous nanometer-sized grains connected by interfaces (called glass/glass interfaces), introducing significant heterogeneity into the isotropic amorphous architecture [27–29]. Compared with the rapid-quenched MG analogues, NGs possess loosely packed interfacial regions with a larger amount of low-coordinated atoms and higher energy states [30], resulting in superior mechanical [31], biochemical [32], magnetic [33], and electrochemical properties [34,35]. Nevertheless, most of the NGs extensively studied are binary or ternary alloy systems. Owing to the restriction of synthesis methods, the bulk NGs consisting of over 5 elements have not been systematically researched, which probably have better catalytic performances due to the synergistic effect of the complex elements.

Here, we first report a multi-element nanoglass (m-NG) of FeCoCrMoCBY synthesized by combining laser ablation and inert gas condensation methods (Laser-IGC). As a new kind of self-supported electrocatalyst with non-noble elements, the Fe-based m-NG exhibits promising electrochemical activity in acidic HER tests compared with the rapid-quenched MG counterparts. Furthermore, a self-optimization behavior is observed in the m-NG during the durability test, resulting in prominent comprehensive HER performances even surpassing commercial Pt/C catalyst. This work not only provides a novel strategy to significantly improve the catalytic properties by introducing inhomogeneous nanostructures into MGs but also reveals the correlation between energy states and electrocatalytic activity of m-NGs.

2. Materials and methods

2.1. Materials synthesis

FeCoCrMoCBY m-NG samples were fabricated by the Laser-IGC technique. Detailed information on the laser-IGC system and the preparation process is described in Ref. [36]. The $Fe_{41}Co_7Cr_{14}Mo_{15}C_{15}B_6Y_2$ (at%) amorphous alloy was selected as the target material, which is reported to have the good glass-forming ability [37]. The MG target was prepared by arc-melting a mixture of high-purity chemicals and then drop-casting into a copper mold. During the powder production process, the atoms of the target were evaporated by a laser beam and eventually coagulated into nano-sized amorphous particles by colliding with He atoms. Disk-shaped m-NG samples (10 mm in diameter and 200 μm in thickness) were formed by in-situ consolidating the powder at 500 MPa and then at 5 GPa for 3 min. The MG samples with the same composition m-NG were synthesized by arc-melting and drop casting as well. The photographs of as-prepared m-NG and MG samples are demonstrated in Fig. S1 in the Supplementary Material.

2.2. Characterization

The X-ray diffraction (XRD) was performed using a Bruker-AXS D8 Advance X-ray diffractometer (Cu $K\alpha$). The microscopic graphs, energy-dispersive X-ray spectroscopy (EDS) images, and selected area electron diffraction (SAED) patterns were obtained by FEI Talos F200S G2 transmission electron microscope (TEM). The thermograph was measured with a Netzsch DSC 404 F3 high-temperature differential scanning calorimeter (DSC). A CS600 Carbon/Sulfur Determinator was applied to confirm the concentration of C, while other elements were measured by Agilent 725 ICP-OES system. X-ray photoelectron spectroscopy (XPS) tests were conducted using a Thermo Scientific K-Alpha XPS system with a monochromatic Al $K\alpha$ X-ray source. The Brunauer–Emmett–Teller (BET) test was performed using a Quantachrome Autosorb IQ2 advanced micropore size and chemisorption analyzer. The micrographs of surface morphology and the EDS images were measured using a Zeiss Sigma500 field emission scanning electronic microscope (SEM).

2.3. Electrochemical measurements

All the electrochemical measurements were carried out using a CHI600E electrochemical workstation with a standard three-electrode system in 0.5 M H_2SO_4. A saturated calomel electrode and a carbon plate (size 20 mm × 20 mm × 1 mm) were applied as reference and counter electrodes respectively. In order to avoid the disruption caused by the dissolution of the carbon electrode, a two-compartment electrolysis cell and N117 Nafion membranes were used to separate the electrodes. All the potentials presented here were referenced to the reversible hydrogen electrode (RHE) for compensating the solution resistance using the equation of $E_{(\text{vs RHE})} = E_{(\text{vs SCE})} + 0.059 \times \text{pH} + 245\ \text{mV} - IR_s$, where I is the working current and R_s is the electrolyte resistance measured by the electrochemical workstation. To prepare the working electrodes, 20 wt% Pt/C (5 mg) and FeCoCrMoCBY nanoparticles (5 mg) were dispersed respectively in the mixture of ethanol (980 μL) and 5 wt.% nafion solution (20 μL). 10 μL of both catalyst inks were loaded onto the ϕ 5 mm glassy carbon electrodes respectively. In addition, the bulk FeCoCrMoCBY m-NG and MG plates were cut into a size of 5 mm × 10 mm × 0.2 mm and fixed on the electrodes using conductive silver adhesive and Teflon paints respectively.

3. Result and discussion

Fig. 1 is the schematic diagram of the synthesis route of FeCoCrMoCBY m-NG. A FeCoCrMoCBY MG target is evaporated by a pulsed laser and coagulated into nanoparticles in a helium atmosphere. Then the amorphous nano-powder is consolidated into bulk sample using the in-situ compression system. This process endows the m-NG with unique inhomogeneous nanostructures, as illustrated in the center blue circle of Fig. 1 (structure details will be discussed later).

As shown in Fig. 2(a), both XRD patterns of the initial FeCoCrMoCBY m-NG and the corresponding MG have distinctive halo peaks without prominent crystalline peaks, indicating their amorphous structure. The annealed states of both m-NG and MG specimens will be discussed later. DSC thermographs of the Fe-based m-NG and MG samples were measured at a heating rate of 20 K min^{-1}, as shown in Fig. 2(b). The glass transition temperature (T_g) and the onset temperature of crystallization (T_x) of MG are 825 K and 868 K, respectively. In contrast, the m-NG exhibits a higher T_x of 907 K, while the glass transition in the m-NG is not as pronounced as the MG. In addition, the DSC curve of m-NG demonstrates an obvious exothermic signal ranging from 377 K to 573 K and a continuous exothermal behavior below the T_x, indicating that the m-NG goes through a structural relaxation during this temperature range, while no similar behavior is observed in MG. The relaxation represents the atomic diffusion and rearrangement

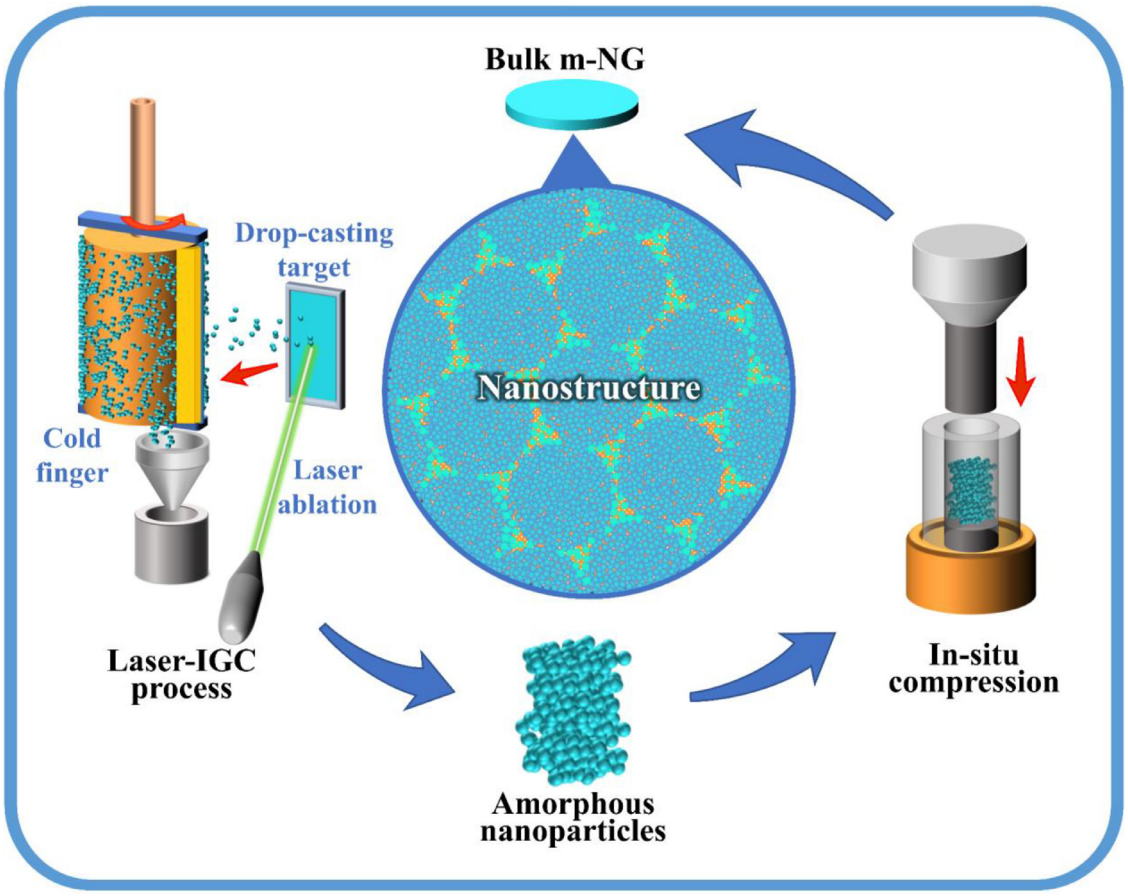

Fig. 1. Schematic illustration of the fabrication process of the FeCoCrMoCBY m-NG.

processes, implying amounts of loosely packed regions, i.e., free volume, existing in m-NG. These results indicate that the Fe-based m-NG is in a higher energy state and then structure relaxation can be easily stimulated by thermal energy [38].

Therefore, both the m-NG and the corresponding MG specimens are annealed at 573 K for 2 h. The XRD patterns indicate that both m-NG and MG specimens remain amorphous structures after the annealing without obvious crystallization peaks, further confirming that the thermal signal of m-NG in DSC corresponds with relaxation instead of crystallization. TEM was performed to characterize the microstructure of the m-NG samples before and after annealing. Spherical glassy cores (dark regions) and their interfaces (light regions) originated from in-situ compression of nanoparticles are manifested in Fig. 2(c). High-resolution TEM images in Fig. 2(d) demonstrate that both core and interfacial parts exhibit typically maze-like amorphous atomic structure. The SAED pattern in Fig. 2(f) shows broad diffraction rings, demonstrating the amorphous structure of m-NG. After the low-temperature annealing, the micrograph of the annealed m-NG still remains the unique nanostructure with pronounced glass-glass interfaces in Fig. 2(e). Meanwhile, the amorphous structure of the annealed m-NG further demonstrates that the atomic diffusion and rearrangement processes, instead of devitrification, occur in the temperature range with an exothermic signal in DSC, implying that the m-NG is in a high energy state.

Fast Fourier Transformation (FFT) was applied on the core and interfacial regions in the micrographs of initial and annealed m-NG samples respectively (Fig. S2). The intensity of FFT images is integrated using the Process Diffraction program [39] for detailed comparison. As illustrated in Fig. 2(g), the profiles of core regions display pronounced peaks at a Q value of 28 nm^{-1}, which is absent in that of interfaces, indicating that the local atoms in the glassy cores are more ordered than that in the interfaces [40,41]. At larger Q values (about 40–70 nm^{-1}), the diffraction intensity of initial cores is higher than that of both interfaces and annealed cores, implying that the inter-atomic distance in cores is shorter than interfaces and slightly expanded during the relaxation. Additionally, the curve of annealed interfaces exhibits a hump (marked by an arrow) at the same Q value range, indicating that the average distance between the annealed interfacial atoms is shorter than that in the initial one [40,42]. These results demonstrate that the inter-atomic distances in different regions are homogenized and the atomic distribution in short ranges becomes more ordered during the annealing. The excess free volume initially localized in the glass/glass interfaces spreads out into the cores and annihilates due to the variation of atomic spacing, meanwhile combining with the decline of energy state [27,43].

The high-angle annual dark field (HAADF) TEM image of as-prepared Fe-based m-NG is shown in Fig. 3(a). The alternating dark and bright domains in Fig. 3(a) indicate the inhomogeneity of atomic packing density distributed on a nanometer scale [44]. The energy-dispersive X-ray spectroscopy (EDS) mapping images in Fig. 3(b–h) demonstrate the distribution of different elements. The (Fe, Cr, Co)-rich, and Mo-rich spherical regions are manifested in the images of Fe, Co, Cr, and Mo in Fig. 3(b–e) respectively. The segregation of Y atoms in the interfacial regions around the cores is observed in Fig. 3(f). The distribution of C and B atoms (Fig. 3(g, h)) appears more homogeneous than the other metallic elements. For comparison, the chemical distribution after annealing is illustrated in Fig. S3. The segregation of different elements is

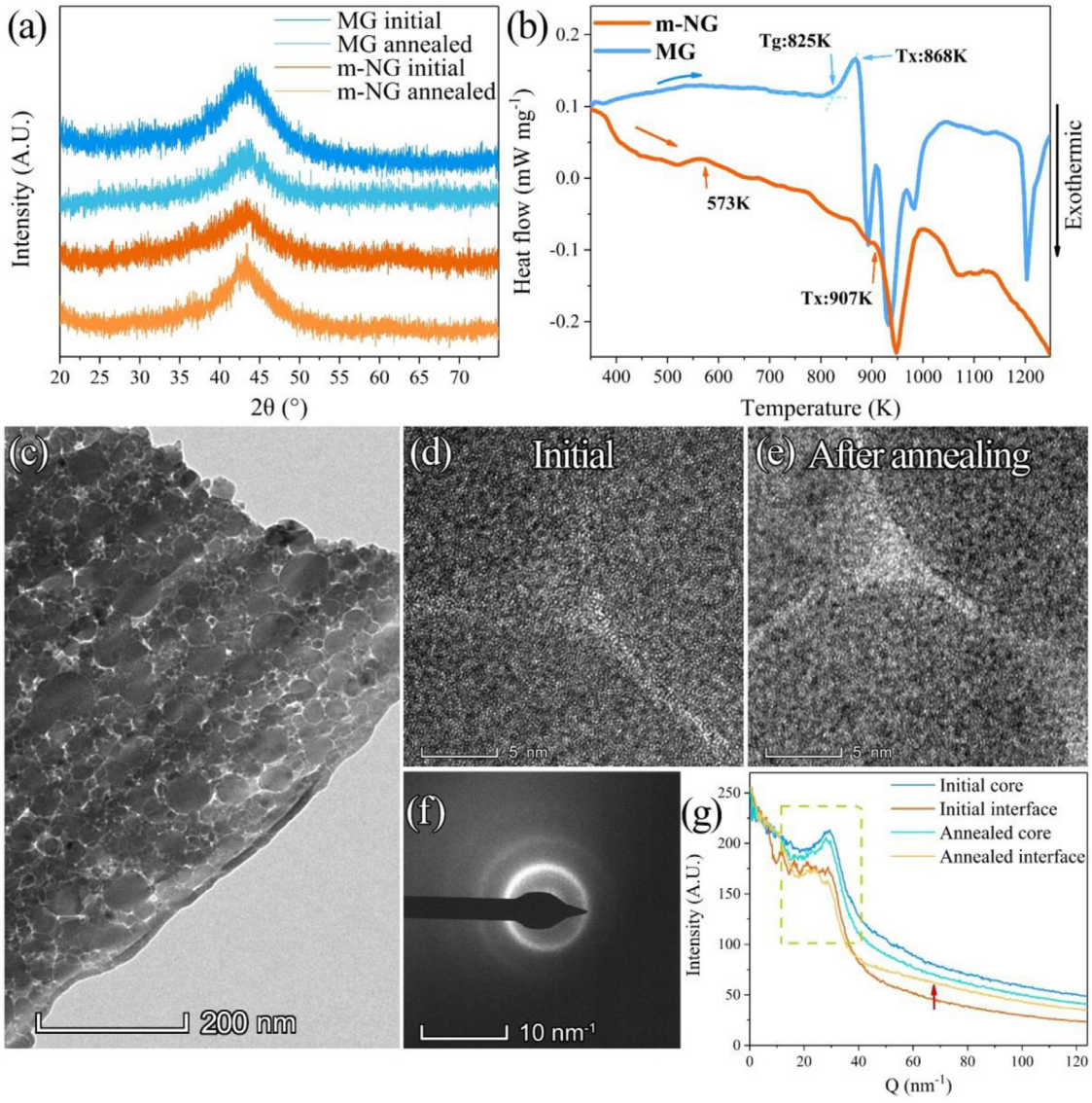

Fig. 2. (a) XRD patterns of the FeCoCrMoCBY m-NG and corresponding MG samples before and after annealing at 573 K for 2 h; (b) DSC curves of the m-NG and MG with a heating rate of 20 K min^{-1}; (c) TEM images of the m-NG sample; (d) high-resolution TEM (HRTEM) image of the m-NG and (e) the annealed samples; (f) the SAED pattern of the m-NG sample; (g) the diffraction patterns obtained by intergrading the intensity of different FFT images.

almost the same as the initial one without any obvious homogenization. Since 573 K is not high enough for long-distance atomic diffusion and phase transformation, the rearrangement of atoms is localized in the form of varying atomic spacing and short-range ordering, leading to the delocalization of the free volume mentioned above. The composition of the Fe-based m-NG sample was measured by combining the ICP-OES and inorganic carbon determination. Compared with the designed target, the m-NG sample has a similar composition with less B, Mo, Fe, and more other elements, as shown in Table S1.

A prominent HER performance is observed in the as-prepared Fe-based m-NG samples measured in 0.5 M H_2SO_4. The details of electrochemical characterization are presented in the experimental section. Linear sweep voltammetry (LSV) was studied with a scan rate of 5 mV s^{-1} on MG, m-NG, and its precursor nanoparticles. According to the polarization curves illustrated in Fig. 4(a), the MG electrodes exhibit sluggish responses to the increasing potential. However, the m-NG exhibits a rapidly increasing electrolyzation current at a much smaller overpotential. The overpotential of m-NG at a current density of 10, 50, and 100 mA cm^{-2} is 62, 152, and 178 mV, respectively, while that of the corresponding MG needs much higher values of 340, 416, and 468 mV, respectively. This phenomenon indicates that the HER catalytic activity of m-NG is superior to MG in acidic solution. Additionally, the LSV profile of the precursor nanoparticles exhibits a moderate catalytic activity with an overpotential of 381 mV at 100 mA cm^{-2} in the same circumstance, implying that the high performance of m-NG originates from its special nanostructure rather than the large surface area of nanoparticles.

After 2-hour annealing at 573 K, the polarization curves demonstrate a severe decline in the catalytic efficiency of m-NG in Fig. 4(b), which can be attributed to the structural relaxation-induced energy reduction mentioned above. The overpotential driving a negative current density of 100 mA cm^{-2} increases from 178 to 378 mV after annealing. For the MG samples, the negative potential only slightly changes from 468 to 483 mV at 100 mA cm^{-2}. To render a deeper insight into the electrocatalytic process, electrochemical impedance spectroscopy (EIS) tests were performed at the open circuit potential from 100 kHz to 0.01 Hz in the 0.5 M H_2SO_4 solution. The Nyquist plots of m-NG and correspond-

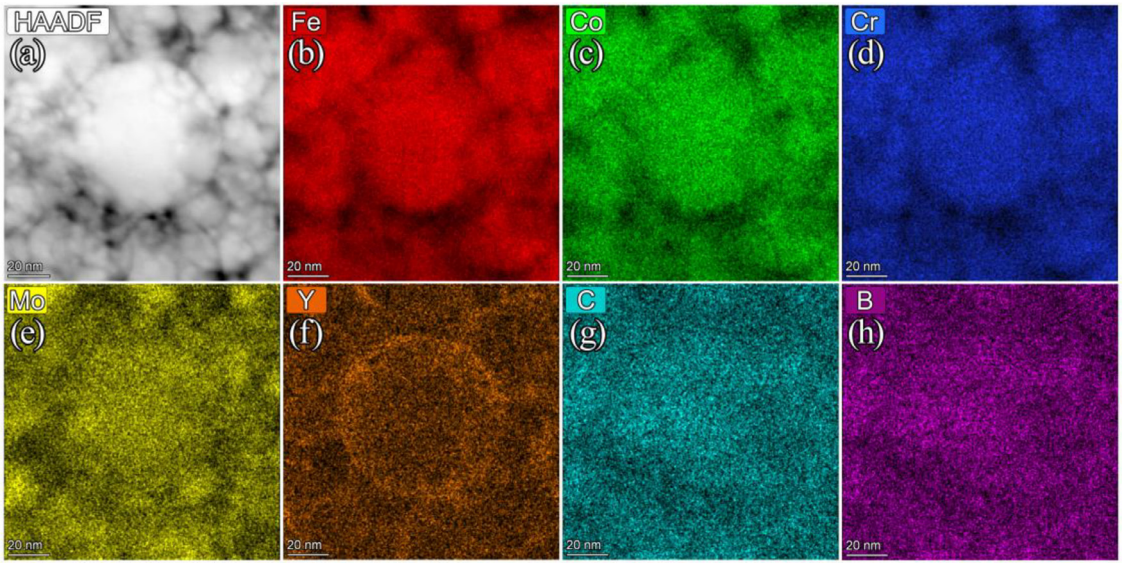

Fig. 3. The chemical distribution of as-prepared FeCoCrMoCBY m-NG. (a) HAADF-STEM image; (b–h) the EDS-mapping images of Fe, Co, Cr, Mo, Y, C, and B elements.

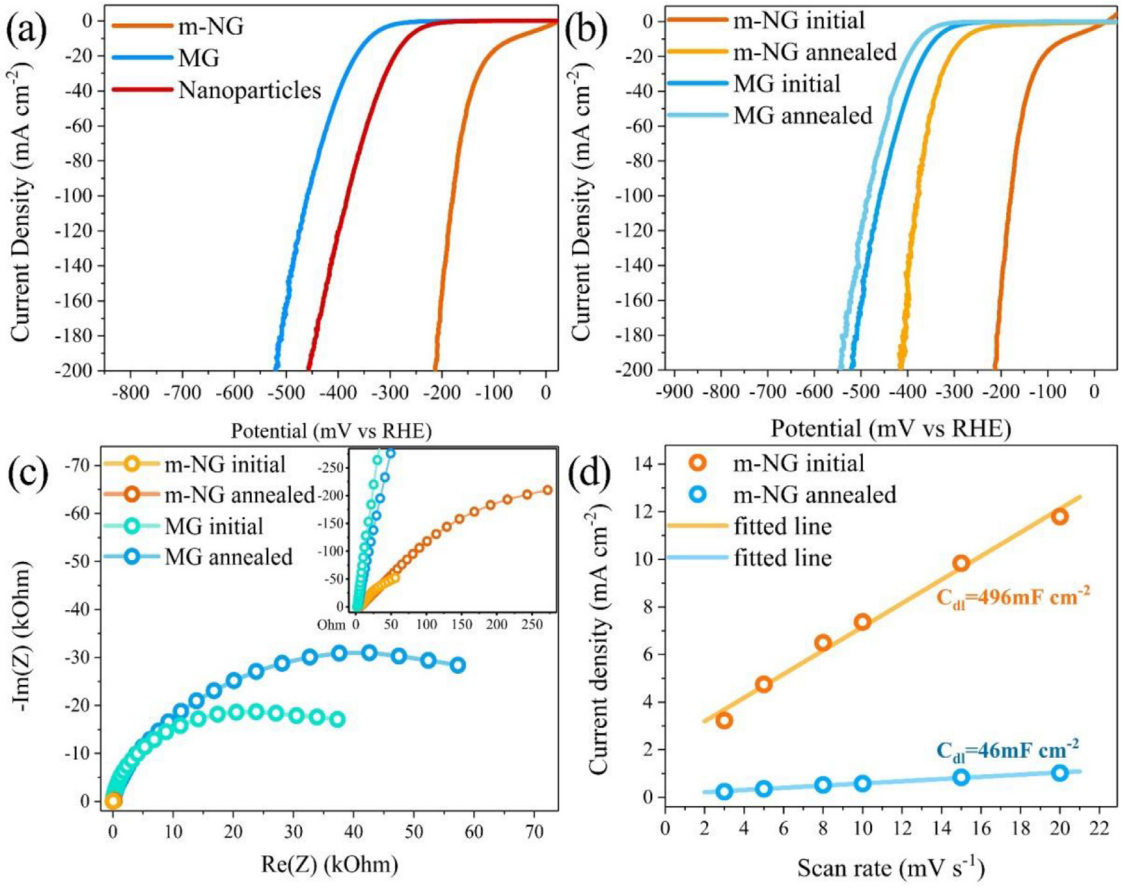

Fig. 4. (a) Polarization curves of MG, m-NG, and corresponding nanoparticles; (b) Polarization curves of m-NG and MG measured before and after annealing; (c) EIS plots for m-NG (insert) and MG measure before and after annealing; (d) the C_{dl} of m-NG extracted from the curves of current density ($\Delta J/2$) vs scan rate.

ing MG in Fig. 4(c) were fitted using equivalent circuit models illustrated in Fig. S4. According to the fitting parameters in Table S2, the charge transfer resistance (R_{ct}) of m-NG is much smaller than that of MG. The small value of R_{ct} indicates a rapid electron transport process and enhanced catalytic kinetics, leading to the better HER performance of m-NG. Besides, the R_{ct} of m-NG increases over 10 times after annealing at 573 K for 2 h, indicating a serious deterioration of electron transportation and catalytic kinetics, which is consistent with the decline of HER activity observed in annealed m-NG.

The electrochemical surface area (ECSA) of the initial and annealed specimens was evaluated according to the double-layer capacitance (C_{dl}) values measured by cyclic voltammetry (CV) curves at different scan rates (Fig. S5), due to the linear proportionality

between C_{dl} and ECSA. As shown in Fig. 4(d), the calculated C_{dl} value of m-NG is 496 mF cm^{-2}, which is obviously higher than that of MG shown in Fig. S6, representing a considerably larger ECSA value of m-NG. After annealing, the C_{dl} of annealed m-NG reduces to 46 mF cm^{-2}, which is less than 10% of that of m-NG, while that of the C_{dl} of annealed MG remains almost unchanged compared with MG. This different behavior between m-NG and MG after annealing represents different structure evolution during annealing, i.e., more free volume annihilation and low coordinated sites disappearance in m-NG, which is consistent with the obvious deterioration of HER performance of annealed m-NG. To understand the probable effect of geometrical surface area on C_{dl}, the specific surface area of m-NG was determined by the nitrogen adsorption/desorption isotherm plots. As illustrated in Fig. S7, the surface area of m-NG is 5.04 m^2 g^{-1} initially and 6.18 m^2 g^{-1} after annealing. Additionally, the pore size distributions of m-NG stay almost the same (Fig. S8), while the specific surface areas become even slightly larger after annealing. Therefore, the decline of ECSA is not caused by the variation of geometrical surface area, which can be attributed to the thermal relaxation, structural homogenization and combined with the amount of low coordinated sites decline mentioned above. It demonstrates the high energy state derived from the heterogeneous nanostructure makes a great contribution to the upgraded HER performance of m-NG compared with the annealed one.

In the long-term characterization, m-NG exhibits prominent comprehensive HER performance even better than the commercial Pt/C catalyst. As illustrated in Fig. 5(a), durability tests of m-NG, MG, and commercial Pt/C catalysts were carried out by means of chronopotentiometry measurement at a constant current density of 50 mA cm^{-2} for 120 h. The overpotential of m-NG decreases obviously from 140 mV to 125 mV at first and then continuously declines with a small slope during the following long-term test. On the contrary, the overpotentials of MG and commercial Pt/C catalysts increase rapidly in the first 20 h and then keep rising over the whole measurement. In only 7.5 h, the overpotential of Pt/C was becoming higher than that of m-NG, representing that the HER activity of m-NG surpasses that of Pt/C during the durability test. After the chronopotentiometry test, the overpotential of m-NG at 100 mA cm^{-2} decreases from 178 to 146 mV, implying that the activity of the m-NG is somehow self-improved.

As illustrated in Fig. 5(b), the LSV curves of m-NG shift toward the direction of smaller negative potential with the increasing circles of CV tests. In contrast, the LSV curves of MG and commercial Pt/C show an opposite trend in Fig. 5(c, d). The overpotential of m-NG driving the current density of j = 100 mA cm^{-2} declines from 178 to 169, 161, and 154 mV after 1000, 5000, and 10000 times of CV cycles in the range of –0.1 V to –0.4 V (vs RHE), while that of MG increases from 468 to 492, 503, and 524 mV under the same circumstance. LSV after 120 h chronopotentiometry test was also conducted, it is inspiring that the overpotential of m-NG is low to 146 mV at 100 mA cm^{-2} much smaller than 360 mV of commercial Pt/C. The overpotentials of all the different samples at j = 10, 50, and 100 mA cm^{-2} are listed in Table S3. Both CV circles and chronopotentiometry tests demonstrate the superior durability and unique self-optimization capability of m-NG.

The Tafel plots are demonstrated in Fig. 5(e). As an intrinsic characteristic of electrocatalysts, the Tafel slope can be calculated by fitting the faradic reaction parts of the LSV curves with the Tafel equation, $\eta = \beta \log j + \alpha$, where η is the overpotential, j is the current density, and β is the Tafel slope. As demonstrated in Fig. 5(e), the Tafel slope of m-NG is 37 mV dec^{-1} initially and then declines to 30 mV dec^{-1} after the durability test, implying that the hydrogen generation process on the surface of m-NG probably corresponds to the Volmer–Heyrovsky mechanism. Moreover, the Tafel slopes of MG and Pt/C have initial values of 82 mV dec^{-1} and 19 mV dec^{-1} and then increase to 104 mV dec^{-1} and 65 mV dec^{-1} after the long-term reaction, respectively, consisting of the decline of their HER activity. Therefore, the m-NG specimens have robust HER performance and higher reactivity than the other specimens after 120 h, implying excellent durability and significant self-optimization ability in acidic solution, which is absent in corresponding MG and commercial Pt/C catalysts. It is worth noting that the prominent HER performance of the non-precious element m-NG is among the group of state-of-the-art catalysts, especially after the long-period durability test (Fig. 5(f) and Table S6).

To investigate the origin of the outstanding durability of m-NG, SEM was carried out to characterize the surface morphology before and after the durability test. As illustrated in Fig. 6(a, b), the surface of MG almost remains unchanged after the long-term reaction, while the m-NG forms a nanoporous structure on the surface. The cross-section images in Fig. 6(c) reveal the nanoporous layer with a thickness of approximately 36 μm. The detailed morphology is illustrated in a cross-section SEM micrograph with higher resolution in Fig. S9. The EDS was also carried out on both m-NG and MG samples to characterize the overall composition before and after the long-term reactions. Considering that the concentration of C is probably disturbed by the adventitious contaminants and B is hardly recognized in the spectrum, the concentration of the other 5 metallic elements are listed in Table S4 along with the EDS spectrum illustrated in Fig. S10. The initial composition of m-NG and MG is close to the design values. After the reaction, the composition of MG stays almost the same as the initial one, consistent with the micrograph in Fig. 6(a). However, the m-NG exhibits a sharp decline in the concentration of Fe and Y elements, while that of Mo increases evidently compared to the initial value. This behavior indicates a selective dissolution of specific elements. The atoms in m-NG have anisotropic chemical states due to the heterogeneous structure, resulting in the various leaching rates of different elements and the formation of galvanic cells, which can accelerate the dealloying process on the surface [45]. Besides, the glass-glass interfaces can serve as the preferential corrosion sites due to the high energy state mentioned above, leading to the unique nanoporous surface morphology. The XRD pattern measured after a 120-h reaction as shown in Fig. S11 exhibits sharp devitrification peaks, matching with (111), (200), and (220) crystal planes of face-centered cubic (FCC) Fe phase. This phenomenon is probably caused by the long-term dealloying process in acidic solution, which destroys the amorphous structure and generates crystalline phases on the surface of m-NG [46–48]. In order to clarify the effects of crystallization behaviors on HER reactivity, both m-NG and MG samples were annealed to 1073 K for 30 min. As illustrated in Fig. S12, both crystallized samples exhibit deteriorated performances, especially for the m-NG, the overpotential driving the current density of j = 100 mA cm^{-2} increases from 178 to 235 mV. This phenomenon suggests that the enhanced catalytic activity of m-NG in long-term reaction is probably not originated from the crystallites on the surface. The dealloying reaction promotes the exposure and utilization of more active sites owing to the enlarged surface areas, corresponding with the self-optimization behavior of m-NG shown in the long-period durability tests. In contrast, the MG is uniformly corroded during the long-term reaction owing to the relatively homogeneous structure originating from the rapid-quenching process.

XPS measurements were performed on the initial and after-HER specimens to investigate the chemical state of the catalysis surfaces of m-NG and MG. The high-resolution spectrum of Fe 2p, Cr 2p, Mo 3d, Co 2p, O 1s, and C 1s are demonstrated in Fig. 6(d–i), while the binding energy of main deconvolution peaks are listed in Table S5. As for the MG, the relative intensity of Fe^0, Cr^0, Co^0, and Mo^0 peaks increases after the reaction along with the negative shift of

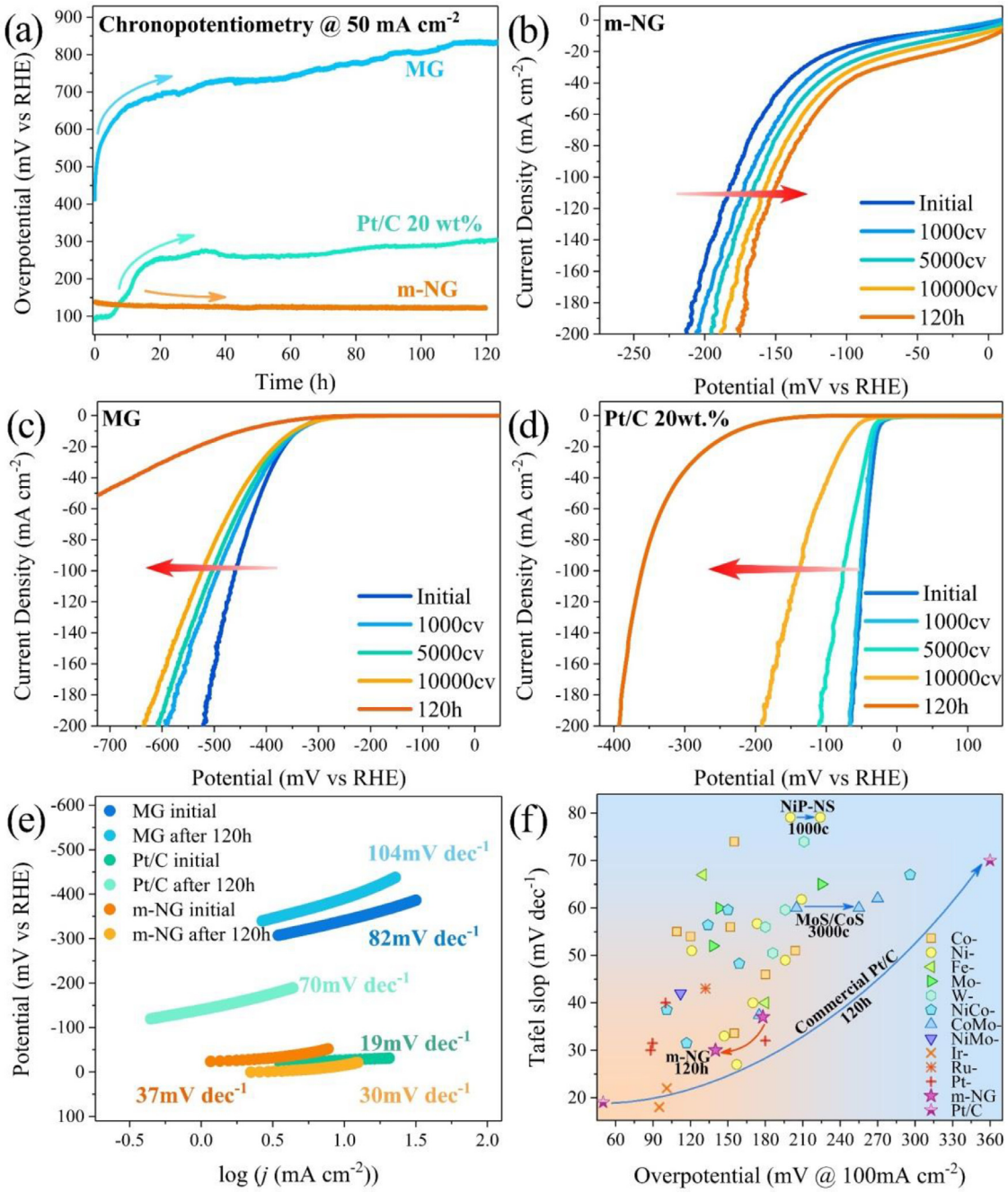

Fig. 5. (a) Time-dependent potential (vs. RHE) plots of m-NG, MG, and commercial Pt/C catalysts; (b–d) Polarization curves of m-NG, MG, and commercial Pt/C measured after different CV circles and durability test; (e) Tafel plots of MG, m-NG, and Pt/C measured before and after durability tests; (f) Tafel slop vs overpotential at 100 mA cm^{-2} for more than 40 kinds of catalysts (e.g., Ni-, Mo-, Co-based catalysts, etc.) for acidic HER.

the spectrum, implying the reduction of metal oxides on the surface of MG, which is in agreement with the decline of metal oxide peak shown in O 1s spectra. The plots of m-NG display a relative decline in the Fe^0, Co^0, Cr^0, and Mo^0 peaks, along with enhanced Fe^{2+}, Fe^{3+}, Co^{2+}, Cr^{3+}, and Mo^{6+} peaks. This variation implies that the metallic elements in m-NG were oxidized during the hydrogen generation process, which is beneficial for upgrading the reactivity. The O 1s plots of m-NG also exhibit an enhancement on the metal oxides peak, which is in agreement with the variations of other metallic elements.

As a consequence, the comprehensive enhancement of the catalytic performances of m-NG can be attributed to the unique nanostructures which is similar to the defects in crystalline catalysts. Heterogeneous defects such as steps, kinks, and edges are usually more reactive than the flat surface [49–51]. Defects could break the periodic structure and modulate the surface electronic structures and energy states by redistributing the localized electrons, leading to the modification of adsorption and activation energy [52]. This endows the atoms in defect sites with preferential adsorption/desorption capability of specific molecules and ions. According to the principles of catalysis, the rate of reactions involving several adsorption species or multistep reactions is closely associated with the most difficult adsorption or desorption process. It is consequently possible to manipulate the reaction rates by altering the energy states and electron structures of the defect sites on the surfaces [53–55]. Additionally, the defect sites with a

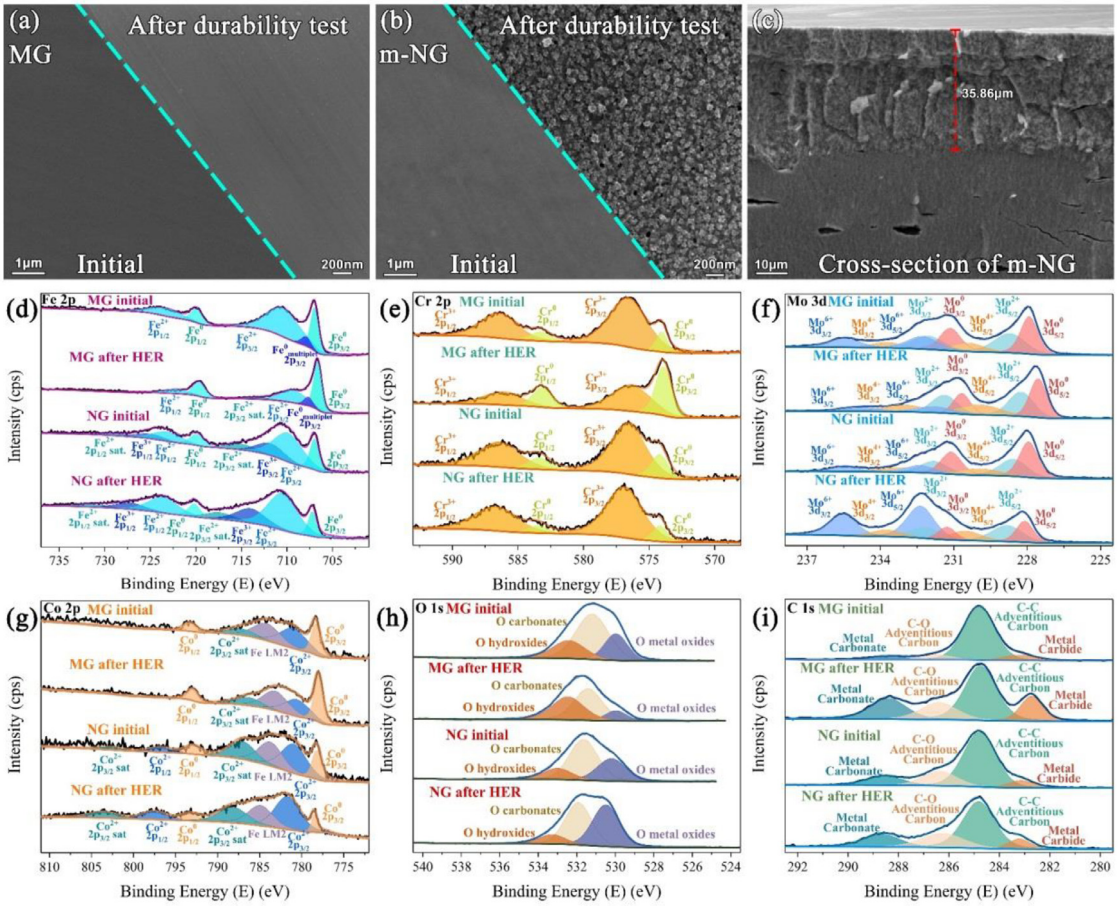

Fig. 6. SEM micrographs and XPS spectra of m-NG and MG samples: (a, b) the high-resolution images of surface morphologies obtained before and after the durability test; (c) the cross-section micrograph of nanoporous layer on the surface of m-NG after the long-term test; (d–i) the XPS high-resolution spectrum measured before and after HER tests.

large number of low-coordinated atoms improve the energy state of surfaces, which reduce the activation energy barriers and upgrade the catalytic reactivity. Therefore, the high-energy surfaces with a high density of defects provide a low-barrier reaction pathway for catalysis processes [56]. For example, it has been determined by a calculation that the reactivity of step sites on Ru(0001) surfaces is over 9 orders of magnitude higher than that of (111) terrace sites in the ammonia synthesis reactions [57]. With respect to m-NG, the low-density interfacial regions introduce significant heterogeneity into the isotropic amorphous matrix of MG, playing a similar character as the defects in the crystalline catalysts. The glass/glass interfaces with excess free volume are originated from the high-pressure consolidation at room temperature, consisting of loosely packed atoms with low coordination numbers. Gibbs free energy of the interfacial atoms is substantially increased due to more disorder packing in the interface region than the adjacent glassy clusters, resulting in a global lower activation energy barrier than that of the rapid-quenched MG [27]. The interfaces can serve as active sites to break the chemical bonds and interact with molecules, ions, and atoms, and the preferential corrosion sites to promote the generation of the nanoporous structures as well. As for the annealed m-NG, although without appreciable crystallization, chemical redistribution, and reduction of specific surface area, it exhibits severe deterioration of HER activity due to the structural homogenization and energy decline observed above. Thus, the glass/glass interfaces play a vital role in the activity of NGs, just like grain boundary and defects in the catalytic performance of crystalline materials.

4. Conclusion

In summary, a multi-element MG, i.e., FeCoCrMoCBY m-NG was successfully fabricated for the first time by the laser-IGC technique. The Fe-based m-NG shows a unique inhomogeneous nanostructure consisting of glassy cores and glass/glass interfaces. The remarkable exothermal behavior accompanying structural relaxation indicates its higher energy states than MG. An outstanding enhancement of HER catalytic activity was discovered on m-NG in the acidic solution, as indicated by a much lower overpotential of 178 mV at 100 mA cm^{-2} than 468 mV of MG. Besides, the m-NG exhibits robust comprehensive performance and self-optimization ability in the long-term tests, even better than the commercial Pt/C catalyst. Our work illustrates that introducing inhomogeneous nanostructure into MG might be an effective method to promote the electrocatalytic properties and reveals the correlation between the energy states and HER catalytic reactivity of the non-precious elements Fe-based m-NG.

Contributions

Mengyang Yan and Shuangqin Chen conceived and carried out the experiments, analyzed the data, charted the figures, and drafted the manuscript. Tao Feng, Si Lan and Horst Hahn advised the synthesis and data analysis and supported the manuscript writing. Shangshu Wu, Xuechun Zhou, and Shu Fu supported the material synthesis experiments. Di Wang and Christian Kübel conducted the TEM test. Tao Feng and Si Lan supervised the project.

All authors contributed to technical discussions and polishing of the manuscript.

Data availability statement

The data that support the findings of this study are available from the corresponding author upon reasonable request

Declaration of Competing Interest

The authors declare that they have no known competing financial interests or personal relationships that could have appeared to influence the work reported in this paper.

Acknowledgments

We acknowledge the support of the Karlsruhe Nano Micro Facility for the microstructure characterization. This work was supported by the National Key R&D Program of China (No. 2021YFB3802800), the National Natural Science Foundation of China (Nos. 52101195, 12261160364, 52222104, 51571119), the Fundamental Research Funds for the Central Universities (Nos. 30919011404, 30920021156, 30919011107), and the Natural Science Foundation of Jiangsu Province (Grant No. BK20200019). T.F. acknowledges the support from the Qing Lan project and the distinguished professor project of Jiangsu province.

References

[1] C.C.L. McCrory, S. Jung, I.M. Ferrer, S.M. Chatman, J.C. Peters, T.F. Jaramillo, J. Am. Chem. Soc. 137 (2015) 4347–4357.
[2] B.P. Setzler, Z. Zhuang, J.A. Wittkopf, Y. Yan, Nat. Nanotechnol. 11 (2016) 1020–1102.
[3] W.J. Jiang, T. Tang, Y. Zhang, J.S. Hu, Acc. Chem. Res. 53 (2020) 1111–1123.
[4] D. Strmcnik, P.P. Lopes, B. Genorio, V.R. Stamenkovic, N.M. Markovic, Nano Energy 29 (2016) 29–36.
[5] F. Yu, L. Yu, I.K. Mishra, Y. Yu, Z.F. Ren, H.Q. Zhou, Mater. Today Phys. 7 (2018) 121–138.
[6] J. Li, G. Doubek, L. McMillon-Brown, A.D. Taylor, Adv. Mater. 31 (2019) e1802120.
[7] Y. Tan, F. Zhu, H. Wang, Y. Tian, A. Hirata, T. Fujita, M. Chen, Adv. Mater. Interfaces 4 (2017) 1601086.
[8] P.G. Debenedetti, F.H. Stillinger, Nature 410 (2001) 259–267.
[9] A.L. Greer, Science 267 (1995) 1947–1953.
[10] Y.F. Wu, W.C. Chiang, J. Chu, T.G. Nieh, Y. Kawamura, J.K. Wu, Mater. Lett. 60 (2006) 2416–2418.
[11] F. Zhang, J. Wu, W. Jiang, Q. Hu, B. Zhang, ACS Appl. Mater. Interfaces 9 (2017) 31340–31344.
[12] Y.C. Hu, Y.Z. Wang, R. Su, C.R. Cao, F. Li, C.W. Sun, Y. Yang, P.F. Guan, D.W. Ding, Z.L. Wang, W.H. Wang, Adv. Mater. 28 (2016) 10293–10297.
[13] S.Q. Chen, M. Li, Q.M. Ji, T. Feng, S. Lan, K.F. Yao, J. Mater. Sci. Technol. 117 (2022) 49–58.
[14] S. Mukherjee, M. Carmo, G. Kumar, R.C. Sekol, A.D. Taylor, J. Schroers, Electrochim. Acta 74 (2012) 145–150.
[15] P. Kolla, A. Smirnova, Electrochim. Acta 182 (2015) 20–30.
[16] M. Carmo, R.C. Sekol, S. Ding, G. Kumar, J. Schroers, A.D. Taylor, ACS Nano 5 (2011) 2979–2983.
[17] B. Hammer, J.K. Nørskov, Adv. Catal. 45 (2000) 71–129.
[18] Y. Li, Q. Zhang, X. Zhao, H. Wu, X. Wang, Y. Zeng, Q. Chen, M. Chen, P. Liu, Adv. Funct. Mater. 33 (2023) 2214124.
[19] Q. Zhang, Y. Hu, H. Wu, X. Zhao, M. Wang, S. Wang, R. Feng, Q. Chen, F. Song, M. Chen, P. Liu, ACS Nano 17 (2023) 1485–1494.
[20] K. Edalati, A. Yamamoto, Z. Horita, T. Ishihara, Scr. Mater. 64 (2011) 880–883.
[21] X. Jian, J. Li, L. He, H.W. Li, M. Zhang, P. Zhang, H.J. Lin, Mater. Trans. 64 (2023) 1515–1525.
[22] D.J. Magagnosc, G. Kumar, J. Schroers, P. Felfer, J.M. Cairney, D.S. Gianola, Acta Mater. 74 (2014) 165–182.
[23] A. Das, E.M. Dufresne, R. Maass, Acta Mater. 196 (2020) 723–732.
[24] F. Chu, B. Han, K. Edalati, J. Ma, Y.Y. Meng, C. Wang, F. Yang, P. Zhang, H.J. Lin, Scr. Mater. 204 (2021) 114145.
[25] K.Y. Wu, Y.Y. Meng, J.C. Xu, K. Edalati, H.Y. Shao, W. Li, H.J. Lin, Scr. Mater. 188 (2020) 135–139.
[26] K.Y. Wu, F. Chu, Y.Y. Meng, K. Edalati, Q.S. Gao, W. Li, H.J. Lin, J. Mater. Chem. A 9 (2021) 12152–12160.
[27] H. Gleiter, T. Schimmel, H. Hahn, Nano Today 9 (2014) 17–68.
[28] H. Gleiter, Small 12 (2016) 2225–2233.
[29] H. Gleiter, Acta Mater. 56 (2008) 5875–5893.
[30] A. Léon, J. Rothe, H. Hahn, H. Gleiter, Rev. Métall. 109 (2012) 35–39.
[31] A. Sharma, S.H. Nandam, H. Hahn, K.E. Prasad, Scr. Mater. 191 (2021) 17–22.
[32] N. Chen, X. Shi, R. Witte, K.S. Nakayama, K. Ohmura, H. Wu, A. Takeuchi, H. Hahn, M. Esashi, H. Gleiter, A. Inoue, D.V. Louzguine, J. Mater. Chem. B 1 (2013) 2568–2574.
[33] C. Wang, X. Mu, M.R. Chellali, A. Kilmametov, Y. Ivanisenko, H. Gleiter, H. Hahn, Scr. Mater. 159 (2019) 109–112.
[34] S. Bag, A. Baksi, S.H. Nandam, D. Wang, X. Ye, J. Ghosh, T. Pradeep, H. Hahn, ACS Nano 14 (2020) 5543–5552.
[35] A. Baksi, S.H. Nandam, D. Wang, R. Kruk, M.R. Chellali, J. Ivanisenko, I. Gallino, H. Hahn, S. Bag, A.C.S. Appl, Nano Mater. 3 (2020) 7252–7259.
[36] J.J. Wang, S.S. Wu, S. Fu, S.N. Liu, M.Y. Yan, Q.Q. Lai, S. Lan, H. Hahn, T. Feng, Scr. Mater. 187 (2020) 335–339.
[37] J. Shen, Q.J. Chen, J.F. Sun, H.B. Fan, G. Wang, Appl. Phys. Lett. 86 (2005) 151907.
[38] Y. Sun, A. Concustell, A.L. Greer, Nat. Rev. Mater. 1 (2016) 1603.
[39] J.L. Labar, Ultramicroscopy 103 (2005) 237–249.
[40] C. Wang, Z.Z. Yang, T. Ma, Y.T. Sun, Y.Y. Yin, Y. Gong, L. Gu, P. Wen, P.W. Zhu, Y.W. Long, X.H. Yu, C.Q. Jin, W.H. Wang, H.Y. Bai, Appl. Phys. Lett. 110 (2017) 111901.
[41] K. Sun, L.M. Xu, H. Weber, G. Wang, J.C. Tseng, J. Shen, S.W. Wu, X.L. Bian, K. Kosiba, U. Kuhn, S. Pauly, Mater. Charact. 178 (2021) 111214.
[42] S. Sohrabi, M.C. Ri, H.Y. Jiang, L. Gu, P. Wen, Y.H. Sun, W.H. Wang, Intermetallics 111 (2019) 106497.
[43] J.X. Fang, U. Vainio, W. Puff, R. Wurschum, X.L. Wang, D. Wang, M. Ghafari, F. Jiang, J. Sun, H. Hahn, H. Gleiter, Nano Lett. 12 (2012) 458–463.
[44] P.D. Nellist, S.J. Pennycook, Adv. Imag. Elect. Phys. 113 (2000) 147–203.
[45] P. Liu, Q. Chen, Y. Ito, J. Han, S. Chu, X. Wang, K.M. Reddy, S. Song, A. Hirata, M. Chen, Nano Lett. 20 (2020) 1944–1951.
[46] X. Wang, R. Li, Z. Li, R. Xiao, X.B. Chen, T. Zhang, J. Mater. Chem. B 7 (2019) 4169–4417.
[47] R. Li, N. Wu, J. Liu, Y. Jin, X.B. Chen, T. Zhang, Corros. Sci. 119 (2017) 23–32.
[48] Y. Li, X. Han, Z. Lu, L. Ying, X. Wang, Y. Zeng, Y. Gao, Q. Chen, P. Liu, Acta Mater. 245 (2023) 11861.
[49] N.P. Lebedeva, A. Rodes, J.M. Feliu, M.T.M. Koper, R.A. van Santen, J. Phys. Chem. B 106 (2002) 9863–9872.
[50] Q. Chen, Y. Jia, S. Xie, Z. Xie, Chem. Soc. Rev. 45 (2016) 3207–3220.
[51] J.L. Gland, V.N. Korchak, Surf. Sci. 75 (1978) 733–750.
[52] P. Liu, P. Guan, A. Hirata, L. Zhang, L. Chen, Y. Wen, Y. Ding, T. Fujita, J. Erlebacher, M. Chen, Adv. Mater. 28 (2016) 1753 –175.
[53] T. Zambelli, J. Wintterlin, J. Trost, G. Ertl, Science 273 (1996) 1688–1690.
[54] Q.S. Chen, A. Berna, V. Climent, S.G. Sun, J.M. Feliu, Phys. Chem. Chem. Phys. 12 (2010) 11407 –1141.
[55] C. Xie, D.F. Yan, W. Chen, Y.Q. Zou, R. Chen, S.Q. Zang, Y.Y. Wang, X.D. Yao, S.Y. Wang, Mater. Today 31 (2019) 47–68.
[56] W.J. Zhu, L. Zhang, P.P. Yang, C.L. Hu, H. Dong, Z.J. Zhao, R.T. Mu, J.L. Gong, ACS Energy Lett. 3 (2018) 2144–2149.
[57] K. Honkala, A. Hellman, I.N. Remediakis, A. Logadottir, A. Carlsson, S. Dahl, C.H. Christensen, J.K. Norskov, Science 307 (2005) 555–558.